Article

Testing the Radiometric Performance of Digital Photogrammetric Images: Vicarious vs. Laboratory Calibration on the Leica ADS40, a Study in Spain

DAVID HERNÁNDEZ-LÓPEZ & BEATRIZ FELIPE-GARCÍA, Albacete, NILDA SÁNCHEZ, DIEGO GONZÁLEZ-AGUILERA & JAVIER GOMEZ-LAHOZ, Salamanca, Spain

Summary: This paper deals with the vicarious calibration of a linear array sensor, ADS40, and the comparison and analysis with the laboratory calibration provided by the manufacturer. For this purpose, a specific test field located in the city of Ávila (Spain) was designed for the two different flights performed during the 8th and 9th of April, 2010 with a spatial resolution of 10 cm and 25 cm, respectively. In addition, a reflectance measurement campaign was performed during the flight using an ASD FieldSpec 3 Hi-Res spectroradiometer, observing a group of 24 targets which included natural and artificial surfaces. Two study cases were considered: with and without atmospheric correction. In order to take into account atmospheric effects, the reflectance method based on the radiative transfer model was applied to establish the relationship between sensor and ground magnitudes. Compared to the calibration results provided by the manufacturer, the results of the vicarious calibration are better. In particular, the root-mean-square grey value error (RMSE) reached through the vicarious calibration in the different reference surfaces is lower than for the laboratory calibration, which considers always the same atmospheric model. Finally, analyzing the stability of the calibration and its relation with the flying height, the calibration of the lower flight (10 cm) was extrapolated to the 25 cm flight, obtaining similar accuracies.

Zusammenfassung: Dieser Artikel beschäftigt sich mit der Feldkalibrierung (vicarious calibration) der Luftbildzeilenkamera ADS40 und vergleicht die Ergebnisse mit denen der vom Hersteller gelieferten Laborkalibrierung. Zu diesem Zweck wurde in Ávila (Spanien) ein Testfeld angelegt, das am 8. und 9. April 2010 in zwei verschiedenen Höhen so überflogen wurde, dass eine Bodenauflösung (Ground Sample Distance, GSD) von 10 cm bzw. 25 cm entstand. Gleichzeitig mit der Überfliegung wurden 24 radiometrische Referenzflächen, die sowohl natürliche als auch künstliche Oberflächen besaßen, vermessen. Dabei kam das Feldspektrometer FieldSpec 3 Hi-Res der Firma ASD zum Einsatz. Die aufgenommenen Kanäle wurden sowohl unter Berücksichtigung eines Atmosphärenmodells als auch ohne ein solches ausgewertet. Als Atmosphärenmodell wurde das 6S (Second simulation of the satellite signal in the solar spectrum), Version 1.1, verwendet. Die Genauigkeit der Feldkalibrierung war etwas höher als die der Laborkalibrierung des Herstellers. Das zeigte sich insbesondere bei unterschiedlichen Oberflächenmaterialien. Ein weiteres Ergebnis war, dass die Ergebnisse der Kalibrierung des niedrigeren Fluges (GSD 10 cm) mit nur einem geringen Genauigkeitsverlust auf die größere Flughöhe (GSD 25 cm) extrapoliert werden konnten.

1 Introduction

Nowadays, the exploitation of physical quantities is still not widespread in thematic applications of aerial images captured by photogrammetric techniques. Nevertheless, as long as the sensor is properly calibrated, it is possible to obtain absolute values of radiance or reflectance, and therefore, these sensors can be used for multispectral classification, vegetation rate calculation and estimation of biophysical variables, providing the advantage over the satellite systems of offering high resolution images and allowing a data acquisition depending

on user demand (Honkavaara & Markelin 2007).

In 2000, Leica Geosystems introduced the photogrammetric scanning sensor ADS40 (Sandau et al. 2000). This camera is innovative in the field of photogrammetry, not only due to its linear sensor characteristics, but also because of the camera manufacturer provides information about the laboratory radiometric calibration (Beisl et al. 2006), and because the application of some atmospheric correction algorithms and an empirical bidirectional reflectance distribution function (BRDF) correction are part of the photogrammetric workflow provided by the manufacturer's software (Beisl et al. 2008).

There are various radiometric calibration methods in remote sensing (de Vries et al. 2007, Honkavaara et al. 2009, Kaasalainen et al. 2009), but the basic principles are the same (Wagner 2010). While the radiometric processing chain is popular for remote sensing systems, those approaches are not directly applicable in photogrammetric processing due to special features of photogrammetric data acquisition (Read & Graham 2002). In remote sensing, here are three types of radiometric calibration of optical sensors (Dinguirard & Slater 1999, Honkavaara et al. 2009, Wagner 2010): pre-flight (at laboratory with Lambertian or spherical reflectors), on board (taking regular measurements of stable targets) and vicarious (based on object pseudo-invariant reflectance).

The radiometric processing methods of photogrammetric imagery are under development, and several organizations are currently developing radiometric block adjustment software (Honkavaara et al. 2009), specifically for photogrammetric sensors. In a vicarious calibration and validation, the test site performance becomes relevant and must be assessed, although optimal construction of permanent radiometric test sites for high resolution airborne imaging systems is an unresolved issue (Honkavaara et al. 2010). Ideally, the field targets used in radiometric calibration either for satellite or airborne sensors should accomplish a set of characteristics (Teillet et al. 2007, Honkavaara et al. 2010). Specially for the latter ones, the requirements related to stability, location, terrain height and climate/

atmospheric properties are the most difficult to realize, i.e., uniformity, sufficiently large footprint, flatness, high signal-to-noise ratio, Lambertian reflectance, as well as minimizing aerosols, water vapour and clouds. Natural and/or anthropogenic targets are used frequently, i.e., rocks or gravel parcels, concrete areas (which can also be painted), sand etc. Specific artificial targets are also common, i.e., transportable tarpaulins or carpets etc.

The authors of this paper conducted some preliminary experiments for radiometric calibration of aerial images with the Intergraph DMC frame camera, analyzing the incorporation of radiometric transfer models into the conventional photogrammetric process (Hernández-López et al. 2011). Recently, very interesting studies on the validation of the radiometric processing chain (Markelin et al. 2010) and the reflectance calibration of the ADS40 were performed (Beisl & Adiguezel 2010). Some of the products processed with the Leica software are evaluated by using ground reflectance measurements as a reference. The results show a reasonably good agreement between the calibration results and the reference.

This article presents an experiment carried out in Ávila (Spain) with the ADS40 sensor. The experiment compared the vicarious calibration of two different flights (10 cm and 25 cm GSD, ground sample distance) with the laboratory calibration provided by the manufacturer: with and without atmospheric correction. A series of check surfaces with different properties have been established for the validation process. During the whole study, the analysis was always based on the Level 0 (L0, raw data) images in nadir direction, without compression and without any geometric or radiometric processing.

This study advances in the research directions raised by the EuroSDR project "Radiometric aspects of digital photogrammetry images" (Honkavaara et al. 2011), which focused on the convenience of performing vicarious calibrations. The main scientific contribution of this work is that remote sensing methodologies for radiometric calibration are adapted, extrapolated and applied to a photogrammetric linear array sensor. Methodologically this implies the application of a rigorous photogrammetric model of the observation

geometry to obtain the geometrical parameters required for atmospheric correction. We also carry out an experimental validation of our method, comparing the vicarious calibration to the laboratory calibration and assessing the influence of atmospheric correction (second simulation of the satellite signal in the solar spectrum (6S) model) on the results.

2   Materials and Methods

2.1 Photogrammetric linear Sensor ADS40-SH52

The sensor used was the Leica ADS40-SH52, with 62.7 mm focal length, 6.5 μm pixel size, a 12,000 pixels array, and a field of view of 64°. It has four panchromatic CCDs: one oriented forward by 27°, one oriented backwards by 16°, and two nadir views at 2°. It also has four multispectral CCDs: red (R), green (G), blue (B) and near infrared (NIR), providing views that are 2° off nadir. The bandwidths are 465–680 nm for the panchromatic channel, 428–492 nm for the blue band, 533–587 nm for the green band, 608–662 nm for the red band, and 833–887 nm for the infrared band, without overlap between bands (CASELLA et al. 2008, MARKELIN et al. 2010).

The camera was calibrated in November 2007 in a laboratory with a uniform white target and an integrating sphere. The calibration parameters are available from Leica on request (BEISL et al. 2006).

2.2 Photogrammetric Flights

The city of Ávila, located 100 km from Madrid, was chosen as a test area. In this area, the conditions for photogrammetric flights are favourable due the cleanness of the air in this region. Furthermore, the area comprises an urban area, but also the surroundings including agricultural vegetation, so it has a large size and radiometric range.

The images used in the calibration process were captured on April 8th, 2010 with an excellent illumination and a clean atmosphere. The flight was conducted at 1000 m flying height, resulting in a GSD of 10 cm, distributed in 7 strips in East-West direction and one in North-South over the test field. The area covered was approximately 22 km². A flight over the same area with a GSD of 25 cm was performed at the next day, 9th of April, with a flying height of 2500 m, distributed in 10 strips in East-West and another one in North-South direction. The covered area is 75 km² (Fig. 1). We worked with images in Level 0 (L0, raw data) of RGB and NIR bands, all of them in the close nadir direction, with 12-bit radiometric resolution.

2.3 Radiometric Campaign

The calibration zone was equipped with seven portable reflectance tarpaulins. Six tarpaulins had different spot colours: black, white, blue, red, green and gray, with a size of 5 × 5 m². The seventh was a 6-step grey-scale tarpaulin
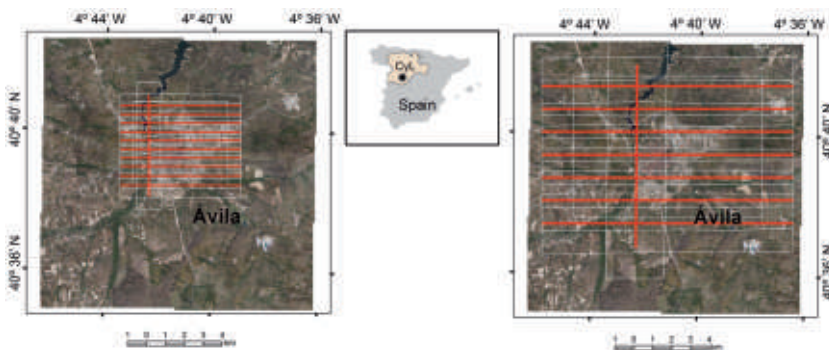

Fig. 1: Flight patterns: GSD of 10 cm on left and of 25 cm on right with control strip in N-S direction in both flights, CyL = Castilla y León.

of 5×1 m² (Fig. 2). These tarpaulins (12 targets) were used as control surfaces to perform the calibration process. The number of spectrometer measurements was 5 in each big tarpaulin and 10 in every step of grey-scale tarpaulin.

In addition, 12 check areas were selected for validation (Fig. 3). Three check areas were natural surfaces, covered by sand, grass and a track. Seven check areas corresponded to artificial surfaces of different colours, namely green, white, garnet and the colour of football soil, and to different materials, namely asphalt, concrete soil and cement. The last two check areas corresponded to paved ground and bushes. Their homogeneity was lower than the homogeneity of the other check areas, but their presence is quite common in the

study area. All the 12 check areas were used in the validation process.

In order to acquire spectral measurements in the field, an ASD FieldSpec3 spectroradiometer was used as a remote detector of the radiant flux coming from the surface in the visible and near infrared ranges. This model provides a spectral range of 350–2500 nm, a data sampling time of 0.1 seconds per spectrum, and a maximum spectral resolution of 3 nm (±1.0 nm wavelength accuracy) with a maximum noise equivalent radiance of 1.4 10^{-9} W·cm^{-2}·sr^{-1}. The optical fiber was mounted with a 25° field of view registering. In the check areas we defined between one and five check targets, each corresponding to a small patch of approximately 1×1 m². In each observation cycle, 120 spectra were measured over each target and then averaged to get the

Fig. 2: Test field: Calibration surfaces.

Fig. 3: Examples for targets (1×1 m^2) in the check areas and the number of reflectance values derived from spectrometer measurements per check area between brackets. As there are five measurements per target, the number of targets per check area is the number of measurements divided by five. For instance, there was one target over sand, but five targets over grass.
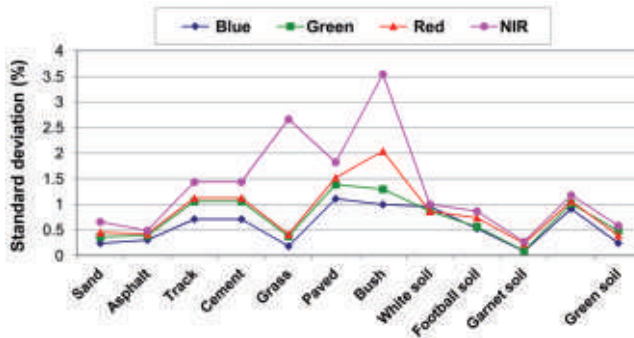

Fig. 4: Standard deviation of measurements (reflectances in %) on the check surfaces.

final spectra. Before each target measurement, a reference measurement was made with a calibrated white reference standard (Spectralon Labsphere ®). The spectra were measured in absolute radiance mode. Afterwards, the radiances were scaled with the reference measurements to produce the reflectance values per target. Finally, these target reflectances were weighted with the ADS40 channel spectral sensitivities to get the reflectances per MS channel. This procedure was repeated five times per target to obtain five representative reflectance values per target. The radiometric samples were georeferenced by determining the centres of the respective targets using a dual-frequency GNSS receiver. The accuracy (RMSE) of the target coordinates was better than 0.1 m. Fig. 3 shows examples for targets (1×1 m^2) from each of the check areas and the number of reflectance values per check area used for evaluation. As there were five reflectance values per target, the number of targets per check area is equal to the number of reflectance values divided by five. The overall number of targets in all check areas was 24, and the total number of reflectances measured in the check areas was 120.

Fig. 4 shows the standard deviation of the measurements for each check area. We can observe the highest values in the check area covered by vegetation (grass and bush) in the NIR band. All the spectral measurements per target were used independently for the calibration procedure (in case of the tarpaulins) and for evaluation (targets in check areas). All the targets (calibration or check surfaces) are visible in at least 5 strips. To obtain the corresponding colour vectors in the images, for each image a target appeared in we determined the average digital number per band in a small square window. The size of this window was 7×7 pixels in the images with 10 cm GSD (calibration and validation) and 3×3 pixels in the images with 25 cm GSD.

2.4 *Radiometric Calibration*

Radiative transfer model

The equation of radiative transfer establishes the relation between reflectances measured on the surface and the apparent reflectance at the sensor, taking into account the processes of atmospheric dispersion and absorption (Vermote et al. 2006).

$$\rho_s(\theta_i,\theta_v,\Phi,z_t,z_s) = \rho_a(\theta_i,\theta_v,\Phi,z_s)$$
$$+\frac{\rho_t}{1-S(z_t,z_s)\rho_t}\tau_\downarrow(\theta_i,z_t)\tau_\uparrow(\theta_v,z_s)\tau_g(\theta_i,\theta_v,z_t,z_s)$$

$$(1)$$

In (1), ρ_s is the apparent reflectance at the sensor, ρ_a is the intrinsic reflectance of the atmosphere, S is the atmospheric albedo, τ_g is the global transmittance due to molecular absorption, $\tau_\downarrow$ is the descending transmittance, $\tau^\uparrow$ is the upward transmittance, ρ_t is the target reflectance measured at the surface, θ_i is the zenith angle of the illumination, θ_v is the zenith angle of observation, Φ is the azimuth angle between the plane of observation and the illumination, z_t is the elevation of the ground point and z_s is the altitude of the sensor.

To obtain the atmospheric parameter values necessary to calculate reflectances at the sensor (ρ_a, E_d, S, $\tau_\downarrow$, $\tau^\uparrow$, τ_g) using (1), the model 6S (Vermote et al. 2006) can be used, which requires information about the geometry of illumination and observation (explained in the next section) for each of the target and band image involved in the process. So, θ_i, θ_v, Φ, z_t and z_s will be the input geometric parameters in the model 6S.

If no such atmospheric correction is applied, the sensor and ground reflectance are considered to be equal, in which case (1) is simplified as follows:

$$\rho_s = \rho_t \qquad (2)$$

The apparent reflectance of the sensor ρ_s can also be expressed as a function of the observed digital number (*DN*) recorded by the sensor (Vermote et al. 2006):

$$\rho_s = \frac{\pi L_s}{E_d \cdot \cos\theta_i} = \frac{\pi(c_0 + c_1 \cdot DN)}{E_d \cdot \cos\theta_i}$$
$$\rightarrow c_0 + c_1 \cdot DN = \frac{E_d \cdot \cos\theta_i}{\pi}\rho_s \qquad (3)$$

In (3), L_s is the radiance at the sensor, E_d is the exoatmospheric solar irradiance at the top of the atmosphere (TOA), c_0 (offset) and c_1 (gain) are the calibration coefficients and ρ_s can be obtained either by the 6S model in (1) or by (2).

For the ADS40 sensor, the linear model suggested by the manufacturer is set up in a way that the offset c_0 is corrected by the system during its registration, so it can be set to zero (Beisl 2006). This aspect was checked by the authors. The solution obtained with determining an unknown offset parameter did not result in an improvement, so that a calibration model with only one parameter (the gain c_1) was used in this study. In the calibration process, the reflectance measurements for each target can be transformed to the images via (1) or (2), where they are related to the digital numbers measured in the corresponding image windows and the radiometric calibration coefficient c_1 via (3). Each observed digital number in an image results in one observation equation. This over-determined system is solved by least squares methods (Hernández-López et al. 2011).

In this study, the vicarious calibration is named case '1', referring to the number of coefficients used (only gain) and the calibration of the manufacturer is named case 'M'. If the atmospheric correction is applied the letter 'a' is added. So, case '1' refers to the vicarious calibration without atmospheric correction, case '1a' to the vicarious calibration with atmospheric correction, case 'M' to the calibration provided by the manufacturer without atmospheric correction and case 'Ma' to the calibration provided by the manufacturer with atmospheric correction. In this work, we did not consider the impact of errors in the atmospheric parameters in (1).

Geometry of illumination and observation

To carry out the vicarious calibration with high resolution photogrammetric images it is recommendable to know the three-dimensional geometry of the scene with the highest accuracy possible if atmospheric correction is to be carried out (Hernández-López et al. 2011).

It is not required in the case without atmospheric correction.

The geometry of the scene for each target is defined by the position of the sun, target and sensor.

The GNSS field measurements and the data provided by the flight company are needed to find the three-dimensional geometry of observation, i.e. the relative position between target and sensor. We determined the exterior orientation parameters by aerial triangulation of the L0 images; note that there is an individual set of orientation parameters for each scanline and band: GPS time, position of projection centre (X,Y,Z) and attitude (omega, phi and kappa). In this study, the positions of the (calibration and check) targets were rigorously georeferenced on the ground using a dual-frequency GNSS receiver and back-projected to the L0 images using the orientation parameters. Back-projection requires an iterative process and also a proper handling of structure and image information. To solve this problem, an application based on the ADS Info kit provided by Leica Geosystems was developed (Tempelmann et al. 2005). As a result, we obtain the GPS time for the time each target was imaged and consequently also the projection centre coordinates, which are used to calculate the azimuth and zenith angles of observation between target and sensor required to determine the atmospheric correction parameters in (1). The back-projected points are used to define the $n \times n$ windows to determine the DN values. We do not consider the obliqueness of the terrain since all our targets are in horizontal terrain.

The solar position algorithm (SPA) library (Reda & Andreas 2008) was used to calculate the illumination geometry, relative position between target and sun, expressed as the geodetic azimuth and the zenith angle at the moment of the data acquisition using GPS time

and target position (geodetic latitude, geodetic longitude and orthometric height).

Atmospheric characterization

With regard to the atmospheric parameters, the values of aerosol optical depth (AOD) were taken from AERONET (AERONET 2010). Due to the absence of closer stations, the value of AOD was extracted as the average of the values of the two closest stations, Autilla and Cáceres, both at a distance of 100 km from Ávila.

The cleanness of the atmosphere at the day of the flight was remarkable, so that the AOD values were pretty similar (Tab. 1). The "Midlatitude Summer" atmospheric model and the continental aerosol model (Vermote et al. 2006) were used to obtain the atmospheric parameters (ρ_a, S, $\tau_\downarrow$, $\tau^\uparrow$, τ_g) for each of the test field measurements based on the 6S model, using the geometrical parameters derived in the way explained in the previous section. The effects of the quality of the atmospheric parameters on the calibration results were not considered in this study.

Solution

The calculation of the calibration is composed of an overdetermined system based on the calibration targets (Fig. 2), and takes into account that for each target we obtain one corresponding image observation in each image the target is visible in, using the mean digital number (DN) value of window of 7×7 pixels. All the reflectances measured at ground level (5–10 per target) are transformed to the images using either (1) (with atmospheric correction) or (2) (no atmospheric correction), where the observation equation is given by (3). In the adjustment, the corrected reflectances are considered as the observations, whereas the digital

Tab. 1: Mean AOD calculated from the closest AERONET stations on April 8th, 2010.

Station	Long.	Lat.	AOD			
			B (at 440 nm)	**G** (at 500 nm)	**R** (at 675 nm)	**NIR** (at 870 nm)
Autilla	−4.603	41.997	0.100	0.084	0.059	0.059
Cáceres	−6.343	39.479	0.104	0.100	0.055	0.045
Mean			**0.102**	**0.092**	**0.057**	**0.052**

numbers were used as constants. Consequently, two solutions were obtained, one without atmospheric correction (case '1') and the other with atmospheric correction (case '1a'). In both cases the overdetermined system has 450 observation equations and one unknown gain parameter c_1 per band. Since some outliers could remain in the measurements, the least squares solution is stabilized with the modified Danish robust method (CASPARY 1987, KRARUP et al. 1980).

2.5 *Validation*

In order to evaluate the vicarious calibration method and compare its effectiveness with the one obtained by the laboratory calibration, we applied all calibration parameters to the image observations in the check targets (Fig. 3) to propagate them into ground reflectances. The ground reflectances thus determined were compared to the ground measurements. The check targets were independent and not used in the calibration process. In this way, for each check measurement and image band, the differences between the ground reflectances $\rho_{calculated}$, obtained by applying the results of the vicarious calibration (with and without atmospheric correction) to the grey levels, and the measured ground reflectances $\rho_{measured}$ were examined. Similarly, the same comparison was done with those reflectances obtained by applying the calibration coefficients provided by the manufacturer. In the cases when atmosphere was considered, the sensor reflectances were transformed into ground reflectances using again the atmospheric characterization provided by the 6S model in (1).

To compare the different cases in a global way, considering all the images and all the targets, the root-mean-square error (RMSE) of the reflectance differences expressed in reflectance units (%) was used:

$$RMSE = \sqrt{\frac{1}{N} \sum \left(\rho_{measured} - \rho_{calculated} \right)^2} \qquad (4)$$

where N is the number of image observations for all check targets.

Furthermore, to analyze each check area (corresponding to several targets of the same land cover type) in an independent way, the following values are determined independently for each check area, considering all the images: the maximal and minimal error, standard deviation, average error, the average absolute error value, and the RMSE.

3   **Results**

3.1 *Parameters of Flight Calibration, Flight of 10 cm GSD*

In this process all calibration surface tarps were used. Tab. 2 shows the gain coefficient and the RMSE obtained from the vicarious calibration, with atmospheric correction ('1a') and without it ('1'). The calculated values are slightly higher than those provided by the manufacturer in all bands ('M'). The RMSEs were smaller with atmospheric correction, except for the R band.

3.2 *Validation*

Fig. 5 shows the accuracy of these experiments expressed as the RMSE in which all the targets and all the images are considered. Vicarious calibration ('1' and '1a') exhibits errors between 2 and 2.6 % in the RGB bands and a slightly higher one, 3.5 %, in the NIR

Tab. 2: Gain coefficients ($W \cdot m^{-2} \cdot sr^{-1} \cdot \mu m^{-1} \cdot DN^{-1}$).

	B		G		R		NIR	
	c_0	RMSE	c_0	RMSE	c_0	RMSE	c_0	RMSE
case '1a'	$5.371 \cdot 10^{-5}$	$9.0 \cdot 10^{-8}$	$3.551 \cdot 10^{-5}$	$9.0 \cdot 10^{-8}$	$3.029 \cdot 10^{-5}$	$9.0 \cdot 10^{-8}$	$3.117 \cdot 10^{-5}$	$7.0 \cdot 10^{-8}$
case '1'	$5.677 \cdot 10^{-5}$	$2.3 \cdot 10^{-7}$	$3.745 \cdot 10^{-5}$	$1.2 \cdot 10^{-7}$	$3.095 \cdot 10^{-5}$	$3.0 \cdot 10^{-8}$	$3.225 \cdot 10^{-5}$	$1.5 \cdot 10^{-7}$
case 'M'	$4.65 \cdot 10^{-5}$	–	$3.39 \cdot 10^{-5}$	–	$2.86 \cdot 10^{-5}$	–	$2.78 \cdot 10^{-5}$	–

Tab. 3: Statistics of the errors of the vicarious calibration (case '1a') using the different check surfaces expressed in reflectances (%), max = maximum error, min = minimum error, std = standard deviation, RMSE = root–mean–square error, ave = average error, ave av = average absolute error value.

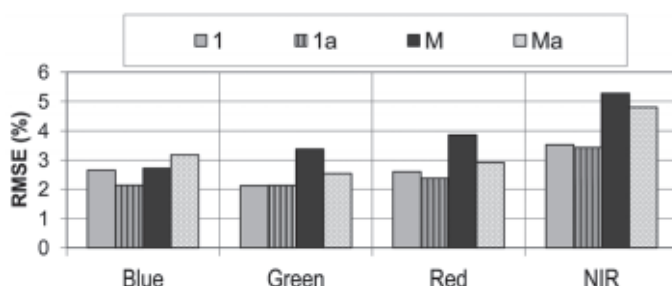| Vicarious		Sand	Asphalt	Track	Cement	Grass	Paved	Bush	White Soil	Football Soil	Garnet Soil	Concrete Soil	Green Soil
Blue	max	3.90	3.73	2.73	2.29	3.72	2.99	4.90	2.68	1.20	2.49	1.22	2.06
	min	−6.04	−0.30	−6.19	−8.75	−2.53	−3.54	−1.40	−6.10	−4.35	−0.06	−4.13	−1.05
	std	2.99	1.01	2.44	2.51	1.36	1.59	1.58	2.02	1.60	0.75	1.34	0.83
	RMSE	2.94	2.02	2.45	3.53	1.87	1.61	1.90	2.22	2.08	1.63	2.05	1.32
	ave	0.01	1.75	−0.41	−2.51	1.29	−0.31	1.10	−0.96	−1.37	1.46	−1.56	1.03
	ave av	2.08	1.77	1.76	2.91	1.75	1.31	1.42	1.77	1.60	1.46	1.73	1.22
Green	max	2.21	4.03	4.55	1.75	2.51	3.50	4.25	6.60	1.66	1.07	1.69	2.60
	min	−6.10	−0.26	−7.32	−8.85	−4.64	−2.39	−2.07	−2.14	−4.84	−0.41	−4.31	−1.61
	std	2.37	1.12	2.89	2.71	1.71	1.48	1.64	2.34	1.92	0.39	1.34	0.94
	RMSE	2.43	1.71	2.90	3.31	1.71	1.49	1.72	3.59	2.00	0.62	1.53	1.48
	ave	−0.69	1.30	0.45	−1.93	0.13	0.26	0.63	2.74	−0.68	0.48	−0.77	1.15
	ave av	1.45	1.34	2.46	2.42	1.34	1.23	1.31	3.00	1.31	0.53	1.18	1.35
Red	max	2.68	3.91	5.14	2.24	2.57	11.84	7.36	7.08	1.06	1.29	2.54	1.49
	min	−7.25	−0.71	−7.63	−9.67	−3.84	−2.12	−4.86	−0.98	−5.12	−2.03	−4.01	−1.77
	std	2.78	1.24	3.08	3.12	1.34	3.45	3.11	2.30	1.63	0.96	1.40	0.74
	RMSE	2.95	1.60	3.13	3.80	1.36	3.60	3.07	3.54	2.07	1.02	1.48	0.84
	ave	−1.12	1.01	0.71	−2.21	−0.22	1.15	0.38	2.70	−1.33	−0.35	−0.50	0.41
	ave av	1.90	1.13	2.75	2.79	1.01	2.06	2.61	2.82	1.52	0.87	1.18	0.71
NIR	max	10.70	2.43	4.82	2.21	8.69	2.87	4.24	5.27	1.41	0.62	4.01	1.86
	min	−7.53	−2.04	−9.28	−6.32	−20.08	−3.45	−13.00	−5.90	−5.00	−3.24	−3.01	−2.22
	std	4.92	1.09	3.29	2.14	5.28	1.47	4.81	2.66	1.86	0.93	1.49	1.03
	RMSE	4.94	1.09	3.27	2.38	5.29	1.55	4.96	2.64	1.94	1.41	1.48	1.04
	ave	1.02	0.14	0.03	−1.07	−0.52	−0.54	−1.55	−0.14	−0.67	−1.07	0.15	0.24
	ave av	3.52	0.85	2.71	1.86	3.95	1.27	3.47	2.17	1.52	1.14	1.11	0.88

Fig. 5: Comparison of the vicarious calibration derived from the 10 cm flight (cases '1' and '1a') and the laboratory calibration (cases 'M' and 'Ma') applied for the 10 cm flight.
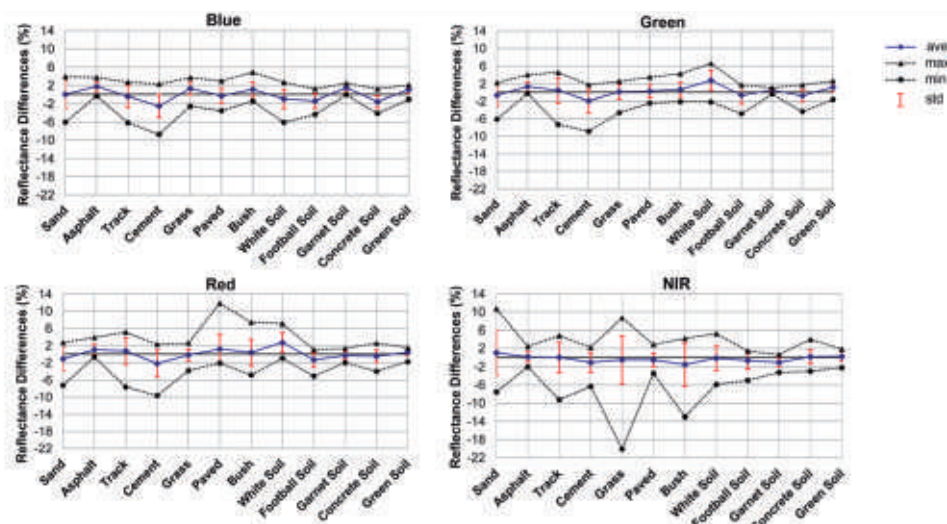

Fig. 6: Maximal and minimal differences between the ground reflectance measurements and those resulting from the vicarious calibration process (case '1a'), with its average and standard deviation (%).

band. The influence of the atmospheric correction in the vicarious calibration was low for all bands, B being the band showing the highest improvement (0.5 %). The RMSEs of the laboratory calibration ('M' and 'Ma') are between 2.6 and 4 % in the RGB band and values close to 5 % in the NIR band. In the case of 'M' the RMSE is higher when the wavelength increases. The results of the calibration coefficients revealed a greater sensitivity to the atmospheric effects ('Ma'), especially in the R and G bands (≈ 1 %). In this case, an increase of the error of 0.5 % for the B band was observed. The RMSEs in reflectances obtained for all the bands after applying the vicarious calibration ('1' and '1a') were smaller than those errors resulting from the laborato-

ry calibration. The NIR band was most significant since it provided an improvement of about 2 %.

Tab. 3 shows the maximum and minimum differences between the ground reflectance measurements at the check surfaces and those resulting from the vicarious calibration with atmospheric correction (case '1a') in absolute terms (expressed in %) and independently for the 12 targets. It shows that the majority of the surface types used as check surfaces may be considered as invariant and suitable for radiometric validation. In general, uniform surfaces that are artificially coloured such as garnet and green provided the best accuracies in the four channels of the spectrum, while more variable surfaces like sand or vegetation had

Tab. 4: Statistics of the errors based on the radiometric manufacturer calibration (case 'Ma') for different check surfaces expressed in reflectances (%), max = maximal error, min = minimal error, std = standard deviation, RMSE = root–mean–square error, ave = average error, ave av = average absolute error value.

ADS40		Sand	Asphalt	Track	Cement	Grass	Paved	Bush	White Soil	Football Soil	Garnet Soil	Concrete Soil	Green Soil
Blue	max	5.52	5.89	5.09	5.85	4.18	6.00	5.93	8.89	3.67	3.32	4.84	3.58
	min	−3.26	1.63	−3.12	−4.48	−1.25	0.37	0.07	0.64	−1.34	1.00	−0.17	0.76
	std	2.62	1.08	2.20	2.35	1.20	1.38	1.47	1.89	1.42	0.68	1.19	0.75
	RMSE	3.31	3.88	3.13	2.77	2.39	3.37	2.79	5.77	1.92	2.45	2.69	2.76
	ave	2.08	3.72	2.25	1.51	2.06	3.09	2.39	5.46	1.32	2.35	2.42	2.66
	ave av	3.08	3.72	2.90	2.30	2.20	3.09	2.39	5.46	1.62	2.35	2.42	2.66
Green	max	3.14	4.76	5.63	3.25	2.76	4.50	4.74	9.10	2.53	1.33	3.29	3.59
	min	−4.86	0.39	−5.95	−7.17	−4.01	−1.01	−1.50	0.49	−3.74	−0.13	−2.82	−0.49
	std	2.28	1.16	2.81	2.67	1.64	1.38	1.62	2.31	1.84	0.39	1.32	0.91
	RMSE	2.26	2.27	3.25	2.66	1.71	1.98	1.97	5.76	1.82	0.84	1.51	2.36
	ave	0.34	1.96	1.66	−0.33	0.50	1.44	1.16	5.29	0.25	0.75	0.75	2.18
	ave av	1.81	1.96	2.91	2.04	1.44	1.62	1.46	5.29	1.50	0.76	1.24	2.21
Red	max	4.03	4.83	6.69	4.22	2.86	12.87	7.84	10.42	2.92	1.76	4.61	2.36
	min	−5.43	0.06	−5.70	−7.43	−3.29	−0.77	−4.03	2.48	−3.03	−1.50	−2.17	−0.77
	std	2.64	1.31	2.98	3.05	1.28	3.30	3.01	2.28	1.55	0.95	1.40	0.71
	RMSE	2.62	2.25	3.83	3.02	1.28	4.15	3.13	6.51	1.64	0.95	1.99	1.49
	ave	0.40	1.84	2.43	−0.08	0.10	2.56	1.06	6.11	0.62	0.15	1.42	1.32
	ave av	2.04	1.84	3.41	2.41	1.02	2.62	2.52	6.11	1.43	0.83	1.67	1.37
NIR	max	13.33	4.22	8.45	6.44	13.57	5.76	6.90	11.56	4.94	1.48	7.68	4.87
	min	−3.18	−0.49	−4.89	−1.85	−13.72	−0.98	−9.05	0.96	−1.01	−2.23	0.01	1.04
	std	4.41	1.18	3.12	2.09	4.94	1.50	4.37	2.54	1.69	0.89	1.71	0.96
	RMSE	6.28	2.08	5.02	3.89	6.44	2.65	4.54	6.87	3.43	0.89	3.85	3.45
	ave	4.55	1.73	3.96	3.29	4.15	2.19	1.51	6.40	3.00	−0.14	3.46	3.32
	ave av	5.34	1.76	4.39	3.51	5.70	2.24	4.04	6.40	3.08	0.72	3.46	3.32

poorer results. These were anisotropic surfaces in which the reflection angles change and the energy that is not gathered by the sensor is lost. That produced a slight increase in its RMSE and standard deviation (std).

The most uniform bands in terms of a similar error were B and G, and the most variable band was NIR (Fig. 6). Here, as expected, the higher error occurred in vegetated samples (bush and grass), because there the NIR band reflectance values and the standard deviation of the measurements were higher.

Next, a comparison with the results obtained using the coefficients of the ADS40 camera and atmospheric correction is done (Tab. 4). In general, for practically all check surfaces the RMSEs of the vicarious calibration are slightly lower than those obtained from the manufacturer calibration coefficients (Fig. 7).

3.3 *Application to 25 cm GSD Flight*

In this section the use of the calibration computed for the 10 cm flight was extrapolated to the 25 cm flight. The main goal was to analyze if it was possible to extrapolate the radiometric results of the vicarious calibration to different ground sample distances and flying heights. The results obtained, considering all the targets and all the images (Fig. 8) show a very similar trend for both flights. In particular, the vicarious calibration exhibited RMSEs lower than 3 % (except for the B band in case '1', where it was 3.5 %). The atmospheric correction in the vicarious calibration improved the results by 1.7 % in the B band, by 0.7 % in the R band and by very small values in the G and NIR bands. The vicarious calibration ('1' and '1a') provided higher precisions than those based on the laboratory calibration ('M' and 'Ma'), with a larger variation for the NIR band of about 2 %. Nevertheless, there was an exception for the B band, which provided a different performance. On one hand, without atmospheric correction, the accuracy of the vicarious calibration ('1') was slightly lower than the laboratory calibration ('M'). On the other hand, the application of the atmospheric correction on the laboratory calibration generated a solution slightly worse than the vicarious one (0.7 %).
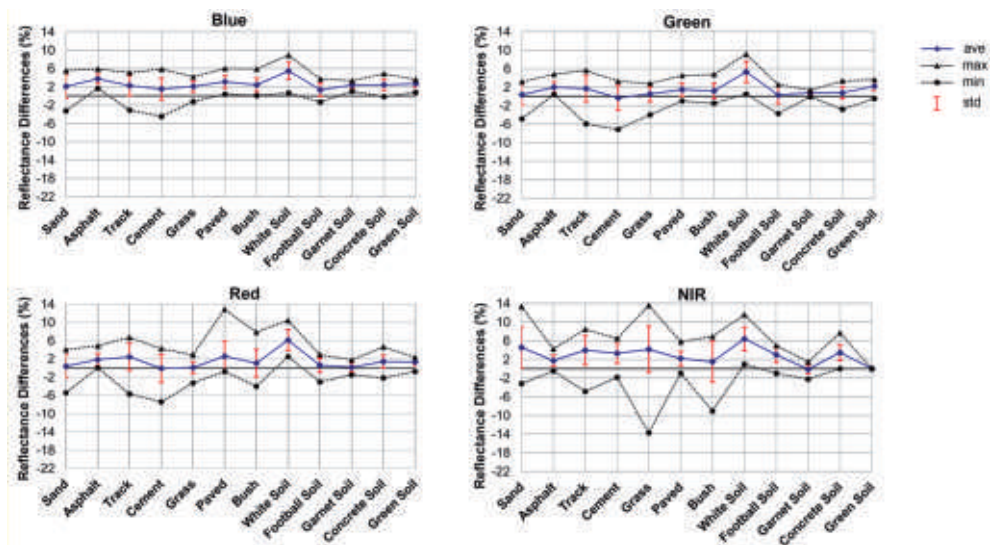

Fig. 7: Maximal and minimal differences between the ground reflectance measurements and the resulting from using the manufacturer calibration coefficients (case 'Ma'), together with its average and standard deviation (%).

4 Discussion

Other authors such as Honkavaara & Markelin (2007) have empirically analysed the spectral response of different airborne sensors through the use of grey patterns located in the field. In particular, they have examined the spectral response of the ADS40, DMC and UltraCamD systems through the use of a pattern with 8 different levels in grey scale. The conclusion is that these systems present an excellent radiometric quality and can be calibrated. The result of this investigation proved the stability of the radiometric laboratory calibration of the ADS40-SH5.

With regard to the calibration surfaces, we used PVC canvases to cope with the requirements mentioned in other works (Honkavaara et al. 2010) and it has been determined that they are suitable for the correct determination of the radiometric camera calibration, in particular ADS40 sensor (Markelin et al. 2010). However, sensor saturations were detected in the original images in some bands for bright objects, though the images have 12 bit dynamic range.

In our investigation raw sensor data have been used, considering the three-dimensional imaging geometry and a digital elevation model. Processing methods relying on the rectification and the consequent resampling of images could involve alterations to the original radiometric information.

The vicarious calibration is of interest in cases when there is doubt as to the calibration values supplied by the manufacturer or when the calibration needs to be validated. The results are consistent with the recently published papers (Markelin et al. 2010, Beisl 2010),

showing that the RMSEs of surfaces reflectances can be better than 5 % in most of the evaluations. The performance varies between the different bands. The performance of the NIR band was lower (3–5 %) than the RGB band in all the cases. The vicarious calibration of the 10 cm flight achieved better results than the laboratory calibration; compared to ground reflectances, RMSEs in the NIR band decreased by about 2 %. In any case, the results achieved for a three-year old laboratory calibration demonstrate the radiometric stability of the sensor. The good weather conditions during the acquisition may have contributed to this result, and thus it would be interesting to repeat the procedure under less favourable conditions. Check surfaces provided large variations in reflectance, depending on the surface and the analyzed band, but they were never above 14 %, reaching even variations lower than 2 % for homogeneous and synthetic surfaces.

The accuracy obtained from the 10 cm calibration flight was preserved in the 25 cm flight. After these experiences, it should be mentioned that the errors increase with the wavelength if the laboratory calibration is used (case 'M'). Likewise, if the atmospheric correction is applied (case 'Ma') the accuracy for the B band gets worse. Therefore, the best solution is the vicarious calibration with atmospheric correction, named here case '1a'. In all the cases, R and G are the most stable bands.

On the other hand, there are some ways for improving the methodology that are worth mentioning: first, concerning the in situ measurements, the atmospheric measurements could be improved. For future work, it would
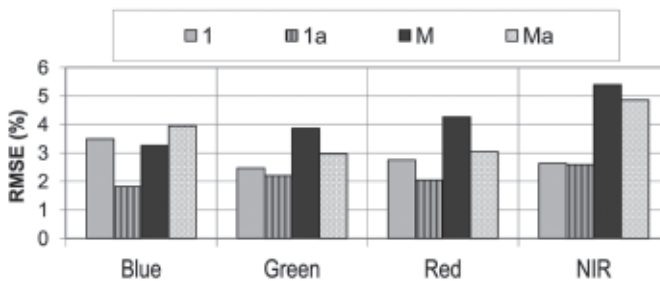

Fig. 8: Comparison of the vicarious calibration derived from the 10 cm flight (cases '1' and '1a') and the laboratory calibration (cases 'M' and 'Ma') applied for the 25 cm flight.

be of interest to analyze the influence of the quality of the meteorological parameters on the final results. Furthermore, it would be interesting to work on the influence of the view direction of the acquisition on the calibration: Although the images were taken approximately in nadir direction (2°) along the flying direction and thus the Lambertian approximation of the surface for the atmospheric correction was applicable, it would be of interest to consider surfaces with an anisotropic behaviour and then analyse bi-directional effects, e.g. applying kernel-driven models (HERNÁN-DEZ-LÓPEZ et al. 2011).

5 Conclusions

In the last years there has without doubt been a convergence between photogrammetric and remote sensing methods for radiometric calibration. This study applied a combination of the photogrammetric principles (collinearity constraint, spatial resection, space intersection, …) according to the mathematical model of this linear sensor to establish the geometrical relations required for radiometric calibration (TEMPELMANN et al. 2005) and the principles of remote sensing, which allow the use of physical models for the image generation, taking into account the problems caused by the atmosphere.

It has been shown that it is possible to perform a radiometric calibration of photogrammetric images through the use of reflectance measurements to obtain and validate the radiometric camera calibration. It has been proven that the solution based on the vicarious calibration with the application of atmospheric correction slightly exceeds the quality of all bands based on the calibration given by the ADS40 sensor manufacturer. However, the ground reflectances obtained from the vicarious calibration and the laboratory calibrations provided by the manufacturer are both acceptable accuracies because the RMSEs achieved by validation for both cases are below 6 %.

It can be concluded that for this investigation, the consideration of atmospheric correction does not affect the results significantly in the imagery acquired at a GSD of 10 cm. Likewise, the use of a vicarious calibration is feasible if it is done shortly before or after the photogrammetric flight, and a different flying height does not significantly affect the results.

The results corroborate the potential of the ADS40 sensor and the need for appropriate laboratory or vicarious calibration to take full advantage of the high radiometric quality of the images.

Acknowledgements

References

AERONET, 2010: Aerosol Robotic Network. – http://aeronet.gsfc.nasa.gov (5.5.2012).

BEISL, U., 2006: Absolute spectroradiometric calibration of the ADS40 sensor. – International Archives of the Photogrammetry, Remote Sensing and Spatial Information Sciences **XXXVI** (1): on CD-ROM, Paris, France.

BEISL, U., TELAAR, J. & SCHÖNERMARK, M.v., 2008: Atmospheric correction, reflectance calibration and BRDF correction for ADS40 image data. – International Archives of the Photogrammetry, Remote Sensing and Spatial Information Sciences **XXXVII** (B7): 7–12.

BEISL, U. & ADIGUEZEL, M., 2010: Validation of the reflectance calibration of the ADS40 airborne sensor using ground reflectance measurements. – ISPRS TC VII Symposium – 100 Years ISPRS, IAPRS **XXXVIII** (7B): 80–85, Vienna, Austria.

CASELLA, V., FRANZINI, M., BANCHINI, G. & GENTILI, G., 2008: Initial evaluation of the second generation Leica ADS40 Camera. – ISPRS Congress Beijing, Commission I, WG **I/4:** 527–532.

CASPARY, W.F., 1987: Concepts of network and deformation analysis. – Monograph **11**, The University of New South Wales, Kensington, N.S.W., Australia.

DE VRIES, C., DANAHER, T., DENHAM, R., SCARTH, P. & PHINN, S., 2007: An operational radiometric calibration procedure for the Landsat sensors based on pseudoinvariant target sites. – Remote Sensing of Environment **107** (3): 414–429.

DINGUIRARD, M. & SLATER, P.N., 1999: Calibration of spatial-multispectral imaging sensors: a review. – Remote Sensing of Environment **68:** 194–205.

HERNÁNDEZ-LÓPEZ, D., FELIPE GARCÍA, B., GONZÁLEZ PIQUERAS, J. & VILLA ALCÁZAR, G., 2011: An approach to the radiometric aerotriangulation of photogrammetric images. – ISPRS Journal of Photogrammetry and Remote Sensing **66** (2011): 883–893.

HONKAVAARA, E. & MARKELIN, L., 2007: Radiometric Performance of Digital Image Data Collection. A Comparison of ADS40/DMC/Ultracam and EmergeDss. – Photogrammetric Week, Stuttgart.

HONKAVAARA, E., ARBIOL, R., MARKELIN, L., MARTINEZ, L., CRAMER, M., BOVET, S., CHANDELIER, L., ILVES, R., KLONUS, S., MARSHAL, P., SCHLÄPFER, D., TABOR, M., THOM, C. & VEJE, N., 2009: Digital Airborne Photogrammetry – A new tool for quantitative remote sensing? A State-of-the-art review on radiometric aspects of digital photogrammetric images. – Remote Sensing **1** (3): 577–605.

HONKAVAARA, E., HAKALA, T., PELTONIEMI, J., SUOMALAINEN, J., AHOKAS, E. & MARKELIN, L., 2010: Analysis of properties of reflectance reference targets for permanent radiometric test sites of high resolution airborne imaging systems. – Remote Sensing **2:** 1892–1917.

HONKAVAARA, E., ARBIOL, R., MARKELIN, L., MARTÍNEZ, L., CRAMER, M., BOVET, S., CHANDELIER, L., ILVES, R., KLONUS, S., MARSHAL, P., SCHLÄPFER, D., TABOR, M., THOM, C. & VEJE, N., 2011: The EuroSDR project Radiometric aspects of digital photogrammetric images. – Results of the empirical phase International Archives of the Photogrammetry. – Remote Sensing and Spatial Information Sciences **38** (Part 4/W19).

KAASALAINEN, S., KROOKS, A., KUKKO, A. & KAARTINEN, H., 2009: Radiometric calibration of terrestrial laser scanners with external reference targets. – Remote Sensing **1** (3): 144–158.

KRARUP, T., KUBIK, K. & JUHL, J., 1980: Gotterdammerung over least squares adjustment. – 14th Congress of the International Society of Photogrammetry **B3:** 369–378, Hamburg.

MARKELIN, L., HONKAVAARA, E., BEISL, U. & KORPELA, I., 2010: Validation of the radiometric processing chain of the Leica ADS40 airborne photogrammetric sensor. – ISPRS TC VII Symposium – 100 Years ISPRS, IAPRS **XXXVIII** (7A): 145–150, Vienna, Austria.

READ, R.E. & GRAHAM, R.W., 2002: Manual of Air Survey: Primary Data Acquisition. – Caithness, Scotland, UK, Whittles Publishing.

REDA, I. & ANDREAS, A., 2008: Solar Position Algorithm for Solar Radiation Applications. – Technical report, National Renewable Energy Laboratory.

SANDAU, R., BRAUNECKER, B., DRIESCHER, H., ECKARDT, A., HILBERT, S., HUTTON, J., KIRCHHOFER, W., LITHOPOULOS, E., REULKE, R. & WICKI, S., 2000: Design principles of the LH systems ADS40 airborne digital sensor. – International Archives of Photogrammetry and Remote Sensing **33** (1): 258–265.

TEILLET, P.M., BARSI, J.A., CHANDER, G. & THOME, K.J., 2007: Prime candidate earth targets for the post-launch radiometric calibration of satellite sensors. – SPIE International Symposium **6677**, San Diego, CA, USA.

TEMPELMANN, U., BORNER, A., CHAPLIN, B., HINSKEN, L., MYKHALEVYCH, B., MILLER, S., RECKE, U., REULKE, R. & UEBBING, R., 2005: Photogrammetric Software for the LH Systems ADS40 Airbone Digital Sensor. – Technical report, Leica Geosystems Geospatial Imaging.

VERMOTE, E.F., TANRÉ, D., DEUZÉ, J.L., HERMAN, M. & MORCRETTE, J.J., 2006: Second Simulation of the Satellite Signal in the Solar Spectrum – Vector (6SV). – 55, Users Guide Version 3.0, University of Maryland, Greenbelt (MD) and Laboratoire d'Optique Atmosphérique, Lille (France).

WAGNER, W., 2010: Radiometric calibration of small-footprint full-waveform airborne laser scanner measurements: Basic physical concepts. – ISPRS Journal of Photogrammetry & Remote Sensing **65:** 505–513.

Addresses of the Authors:

DAVID HERNÁNDEZ-LÓPEZ & BEATRIZ FELIPE-GARCÍA, Regional Development Institute, University of Castilla-La Mancha, Albacete, Spain, e-mail: {david. hernandez}{beatriz.felipe}@uclm.es

NILDA SÁNCHEZ , CIALE, Spanish-Portuguese Centre of Agricultural Research, University of Salamanca, Spain, e-mail: nilda@usal.es

DIEGO GONZÁLEZ-AGUILERA & JAVIER GOMEZ-LAHOZ, Department of Cartographic and Land Engineering, University of Salamanca, Spain, e-mail: {daguilera}{fotod}@usal.es